



Impacts of Climate Change on Atmospheric Rivers over East Asia

Tae-Jun Kim¹ · Jinwon Kim¹ · Jin-Uk Kim¹ · Chu-Yong Chung¹ · Young-Hwa Byun¹

Received: 25 January 2024 / Revised: 24 May 2024 / Accepted: 28 May 2024

© The Author(s) under exclusive licence to Korean Meteorological Society and Springer Nature B.V. 2024

Abstract

Atmospheric rivers (ARs) are closely associated with extreme precipitation and hydrological events in East Asia. Predicting the impacts of climate change on ARs is crucial for preventing the damage caused by extreme precipitation and ensuring the effective operation of water management facilities. We aimed to conduct future projections (2080–2099) of annual and seasonal changes based on the assessment of East Asian AR and AR-related precipitation, using the Coupled Model Inter-comparison Project Phase 6 (CMIP6) Multi-model ensemble (MME). The annual average integrated vapor transport (IVT) in East Asia in 2080–2099 will increase by approximately 32.5% compared to 1995–2014. Meanwhile, the annual average AR frequency (F_{AR}) will increase by approximately 111%. Examination of the water vapor and moist wind components of the IVT revealed that the future increase in the IVT was primarily from increases in water vapor. The increase in IVT is largely responsible for the increase in AR frequency. Changes in AR following global warming have also affected precipitation, increasing the total precipitation for East Asia. An examination of the changes in AR characteristics shows that the frequency of intense AR events will also increase owing to global warming. Increases in the frequency of strong AR events during the East Asian summer monsoon season are projected to occur. Projections regarding the frequency and intensity of AR events vary substantially by region, such as Korean Peninsula, Southern China and Western Japan.

Keywords Atmospheric Rivers · Climate Change · CMIP6 · Multi-model Ensemble · East Asia

1 Introduction

Atmospheric rivers (ARs) are globally and regionally important features that transport poleward moisture transport across the mid-latitudes (DeFlorio et al. 2019; Guan and Waliser 2015; Ionita et al. 2020; Neiman et al. 2008; Zhu and Newell 1998). ARs have long and narrow corridors with strong moisture flux, often leading to considerable precipitation over relatively narrow regions. They are closely associated with extreme hydrological events and the resulting damage (Dettinger et al. 2011; Kim et al. 2013; Lavers et al. 2013; Ralph et al. 2006; Ryu et al. 2021; Whan et al. 2020). In the coastal areas of California, AR-induced precipitation accounts for approximately 20–50% of the annual rainfall and has been linked to flood events and the cessation of droughts (Dettinger et al. 2011; Dettinger 2013; Ralph et al. 2006; Rutz et al. 2014). In western Europe, precipitation

because of ARs comprises approximately 30% of seasonal rainfall and has been associated with annual maximum daily rainfall and flooding (Benedict et al. 2019; Ionita et al. 2020; Lavers et al. 2013, 2015; Whan et al. 2020).

East Asia and the western Pacific coast have been identified as regions that are highly impacted by the AR (Guan and Waliser 2015; Kamae et al. 2017b; Kim et al. 2021, 2023a). East Asia is one of the regions substantially influenced by AR, with AR-induced precipitation accounting for 30–60% of the annual rainfall, and several extreme precipitation events that have led to severe damage in East Asia have been linked to ARs (Guan and Waliser 2019; Kamae et al. 2017a; Kim et al. 2021, 2023a). In East Asia, ARs occur most frequently during the summer, exerting a considerable influence on total precipitation. There is likely a close relationship between summer precipitation band patterns in East Asia and AR occurrence, and the precipitation caused by ARs (Kamae et al. 2017a; Kim et al. 2021, 2023a; Park et al. 2021). However, due to seasonal and geographical differences in climate patterns that are known to primarily affect AR, such as the North Pacific High and the East Asian summer monsoon, the timing of high AR occurrence also varies

✉ Jin-Uk Kim
jukim86@korea.kr

¹ National Institute of Meteorological Sciences, 33, Seohobuk-Ro, Seogwipo-Si, Republic of Korea

within East Asian region (Kim et al. 2021, 2023a; Liang et al. 2023; Pan and Lu 2020). Consequently, further diverse studies on AR specific to the East Asian region are needed.

Leung and Qian (2009), Dettinger (2011), Lavers et al. (2013), and Paltan et al. (2017) have suggested that ARs are associated with the occurrence of floods and the termination of droughts in different regions. This makes it important to project the effects of ongoing climate change on ARs and related hydrology in regions that are heavily affected by ARs. Recent studies, using climate change scenarios such as the Shared Socio-economic Pathways (SSP) of the Coupled Model Intercomparison Project Phase 6 (CMIP6) and previous scenarios, have suggested that AR occurrence and precipitation induced by ARs are projected to increase in the future in various regions such as northwestern North America, Europe, and East Asia (Corringham et al. 2022; Espinoza et al. 2018; Gao et al. 2016; Ishida et al. 2018; Liang and Haywood 2023; Mahoney et al. 2018). Given that AR characteristics are closely associated with heavy rainfall events, extreme rainfall-related damage linked to ARs will likely increase in multiple regions (Corringham et al. 2022; Jeon et al. 2015; Rhoades et al. 2021; Whan et al. 2020). The projected increases in ARs and AR-related precipitation from climate change suggest that floods are likely to occur more frequently and with increased intensity (Allan et al. 2014; Dettinger 2011; Ionita et al. 2020; Lavers et al. 2013; Leung and Qian 2009; Meresa et al. 2022; Paltan et al. 2017; Whan et al. 2020). Understanding the impacts of climate change on regional ARs and associated hydrological phenomena is crucial for the effective planning, construction, maintenance, and operation of water management infrastructure, including reservoirs, dams, and drainage systems, to mitigate the damage caused by extreme rainfall events (Albano et al. 2020; Benedict et al. 2019; Ionita et al. 2020; Lavers et al. 2013; Payne et al. 2020).

Despite the significance of East Asian AR highlighted earlier, research on the outlook of East Asian AR based on SSP scenarios is lacking. Additionally, the studies often limit the analysis seasons to annual or boreal winter and summer, and frequently rely on single models (Liang and Haywood 2023; Wang et al. 2023; Zhang et al. 2024). Considering the significant variations in the impact of AR within the East Asian region across different seasons, it is necessary to conduct seasonal analyses. And utilizing ensemble data can reduce the uncertainty of the models. Therefore, this study aimed to conduct future projections of annual and seasonal changes based on the assessment of East Asian AR and AR-related precipitation, as performed by Kim et al. (2023a), using the CMIP6 Multi-model ensemble (MME). The analysis included examining the impact of wind and humidity on future AR changes, differences based on AR intensity classifications by Ralph et al. (2019), and changes in East Asian precipitation band patterns. Section 2 outlines the data

and methodologies used in this study, and Sect. 3 presents the results of the ARs and their associated variables. The conclusions and discussion are provided in Sect. 4.

2 Data and Methods

In this study, daily data on zonal winds (u), meridional winds (v), specific humidity (q), and precipitation (PR) from historical periods were used along with the SSP5-8.5 scenario assuming rapid advancement in industrial technology with a focus on high fossil fuel usage and uncontrolled urban-centric development expansion (SSP585 hereafter). Typically, 6-hourly data is used for AR detection. However, due to the limited number of models that provide 6-hourly data, we utilized daily data to incorporate a variety of model datasets. In this process, we confirmed that daily data sufficiently represents the climate characteristics of AR by using some models that provide both 6-hourly and daily data (not shown). The data were derived from 15 global climate models (GCMs) from CMIP6 and were used for the analysis of AR detection and AR-related precipitation (Table 1). The climate change (CC) signal was calculated as the average difference between the variables corresponding to a distant future in 2080–2099 and a historical period in 1995–2014, with each spanning 20 years.

To detect ARs using the GCM data, the method proposed by Park et al. (2021) (PSK2021 hereafter) was used. This detection method is based on the method of Guan and Waliser (2015) (GW2015 hereafter). This relies on the characteristics of vertically integrated vapor transport (IVT), as defined in Eq. 1. In Eq. 1, u , v , and q are the previously mentioned variables, and g is the gravitational acceleration. In GW2015, the IVT threshold was defined as exceeding the 85th percentile of a reference period and greater than $100 \text{ kg m}^{-1} \text{ s}^{-1}$. However, in PSK2021, the IVT threshold was modified to an IVT anomaly (IVTA), defined as IVT deviation from the climatological mean, exceeding $150 \text{ kg m}^{-1} \text{ s}^{-1}$. PSK2021 excludes the constraint on the net direction of the IVT, which is restricted to the poleward direction in GW2015. This modification was made because using IVTA more effectively captures extreme rainfall during the East Asian summer monsoon. In addition, the moisture transport accompanying the East Asian summer monsoon-associated ARs sometimes occurs in an east–west direction rather than poleward (Park et al. 2021). These changes in PSK2021 enable a more realistic detection of AR in the East Asian region. The AR detection process in PSK2021 proceeded similarly to that in GW2015. This excluded entities deviating more than 45° from the mean IVT direction or where more than half of the grid points belonging to the AR object deviated more than 45° from the mean IVT direction. ARs with a length of less than 2000 km

Table 1 Resolution and specifics of the CMIP6 GCMs used in this study

Model	Institution	Resolution/Specifics
CanESM5	CCCMA/ECCC	128×64 (T63L49)
CESM2-WACCM	NCAR-CGD	288×192, Finite volume
CMCC-ESM2	CMCC	288×192, Finite volume
CNRM-ESM2-1	CNRM/CERFACS	256×128 (T127L91)
EC-Earth3	SMHI	512×256 (T255L91)
FGOALS-g3	CAS	180×80 (area-weighted Lat–Lon grid)
IITM-ESM	CCCR-IITM	192×94 (T62L63)
INM-CM5-0	INM	180×120 (2°×1.5°)
IPSL-CM6A-LR	IPSL	144×143 (2.5°×1.25°)
KACE-1-0-G	KMA	192×144 (1.875°×1.25°)
MIROC-E2SL	MIROC team	128×64 (T42L40)
MPI-ESM1-2-HR	MPI-M	384×192 (T127L95)
MRI-ESM2-0	MRI	320×160 (T159L80)
NorESM2-MM	NCC	288×192 (1.25°×0.9°), Finite volume
TaiESM1	RCEC	288×192 (1.25°×0.9°), Finite volume

or an aspect ratio of less than 2 were excluded. The monthly occurrence frequency of the detected ARs was defined as the AR frequency (F_{AR}). However, Park et al. (2023) have indicated that the PSK2021 method excessively detects AR in tropical regions. Therefore, in this study, the 10.5°S to 10.5°N region was excluded from the analysis.

To analyze future changes in F_{AR} , the components of IVT were decomposed into contributions from precipitable water vapor (PWV) and wind (UV) factors defined in Eqs. 1–3 below, as outlined by O’Brien et al. (2022). UV represents the contribution of wet wind components, rather than only wind components, to the IVT.

$$\text{IVT} = \sqrt{\left(\frac{1}{g} \int_{1000\text{hPa}}^{300\text{hPa}} qu \, dp\right)^2 + \left(\frac{1}{g} \int_{1000\text{hPa}}^{300\text{hPa}} qv \, dp\right)^2} \quad (1)$$

$$\text{PWV} = \frac{1}{g} \int_{1000\text{hPa}}^{300\text{hPa}} q \, dp \quad (2)$$

$$\text{UV} = \text{IVT}/\text{PWV} \quad (3)$$

Applying the method proposed by Ralph et al. (2019), which categorizes the intensity of AR based on maximum IVT values (250/500/750/1000/1250 kg m⁻¹ s⁻¹) and AR duration (24/48/72 h), AR intensity was classified into five categories, that is, Category 1 (primarily beneficial; Cat 1), Category 2 (mostly beneficial, also hazardous; Cat 2), Category 3 (balance of beneficial and hazardous; Cat 3), Category 4 (mostly hazardous, also beneficial; Cat 4), and Category 5 (primarily hazardous; Cat 5). The method classifies both cases with strong moisture transport in a short time and those with relatively weak moisture transport in a long time as strong AR. The total precipitation during

the AR periods over a span of 20 years, relative to the total precipitation over the same period, was defined as PR_{ARf} .

After each GCM variable was interpolated into the same grid with a 1.5°×1.5° horizontal resolution, the MME was calculated. However, for AR detection in each GCM, to ensure consistency in geometric conditions such as object distance or width, the IVT and IVTA calculated at the horizontal resolution of each GCM were initially interpolated onto a grid with a resolution of 1.5°×1.5° grid cells. The PSK2021 method was then applied to detect the AR data. The details description of the performance evaluation of the MME is provided in Kim et al. (2023a), while the descriptions for individual models are provided in Kim et al. (2023b).

The analysis was conducted over two designated regions, that is, Global (GL) and East Asia (EA). In the analysis of the AR categories, three additional sub-regions, namely, the Korean Peninsula (KOR), western Japan (WJP), and southern China (SCN), were included following the methods of Kim et al. (2023a), to provide regional-specific information. The details of each specific area, excluding the global region, are provided in Table 2.

Table 2 EA, KOR, SCN, WJP regions used in this study

Region	Longitude	Latitude
East Asia (EA)	100.5°E to 180.0°E	21.0°N to 60.0°N
Korean Peninsula (KOR)	124.5°E to 130.5°E	34.5°N to 40.5°N
Southern China (SCN)	108.0°E to 118.5°E	22.5°N to 27.0°N
Western Japan (WJP)	129.0°E to 141.0°E	31.5°N to 37.5°N



3 Results

Figure 1 shows the historical 20-year average, future 20-year average, and future changes (future–historical) in F_{AR} . During the historical period, regions with high F_{AR} were predominantly located in the mid-latitudes of the North Pacific and North Atlantic, and in the Antarctic Sea, exhibiting seasonality (Fig. 1a–b). The area highlighted in the black box, representing the EA region, was influenced by AR activity in the North Pacific during MAM and JJA. During DJF, the AR core, located east of the mid-latitude North Pacific, migrated northward from the western Pacific region during MAM and JJA, thereby impacting the EA region. During JJA, there is a connection in F_{AR} extending from the northern Indian Ocean to the AR core in the mid-latitude North Pacific. In the future, the F_{AR} has been projected to increase while maintaining the seasonal variability observed in the historical period (Fig. 1b). The F_{AR} in the EA region was projected to increase by more than twofold, that is, approximately +111%, compared with that in the historical period, surpassing the global average

increase in F_{AR} (Table 3, GL: +5.42%, EA: +7.12%). The increase in F_{AR} in EA will likely be the highest during JJA (Table 3; DJF: +4.60%, MAM: +7.19%, JJA: +9.74%, SON: +6.89%). Within EA, F_{AR} is expected to increase during MAM and JJA in the southern regions of China. An overall increase in F_{AR} is expected along the East Asian coastlines and in inland China (Fig. 1c).

From left to right, Fig. 2 shows the historical period average of IVT, future changes in IVT, and future changes in IVT specific to EA. The outcomes for the historical and future changes in IVT resemble the spatial and seasonal patterns observed in the F_{AR} illustrated in Fig. 1. However, there was a difference between the F_{AR} in the historical period, which predominantly showed the greatest tendency for this in the mid-latitudes. Meanwhile, IVT had the highest values in tropical regions (Fig. 2a). This suggests that a substantial amount of moisture content in the tropics may not be associated with AR-type water vapor transport (Kim et al. 2023b).

Future changes in IVT were primarily high in mid-latitude and tropical oceans (Fig. 2b). In EA, IVT is projected to increase by approximately 32.5% compared with that in the historical period, with these increases

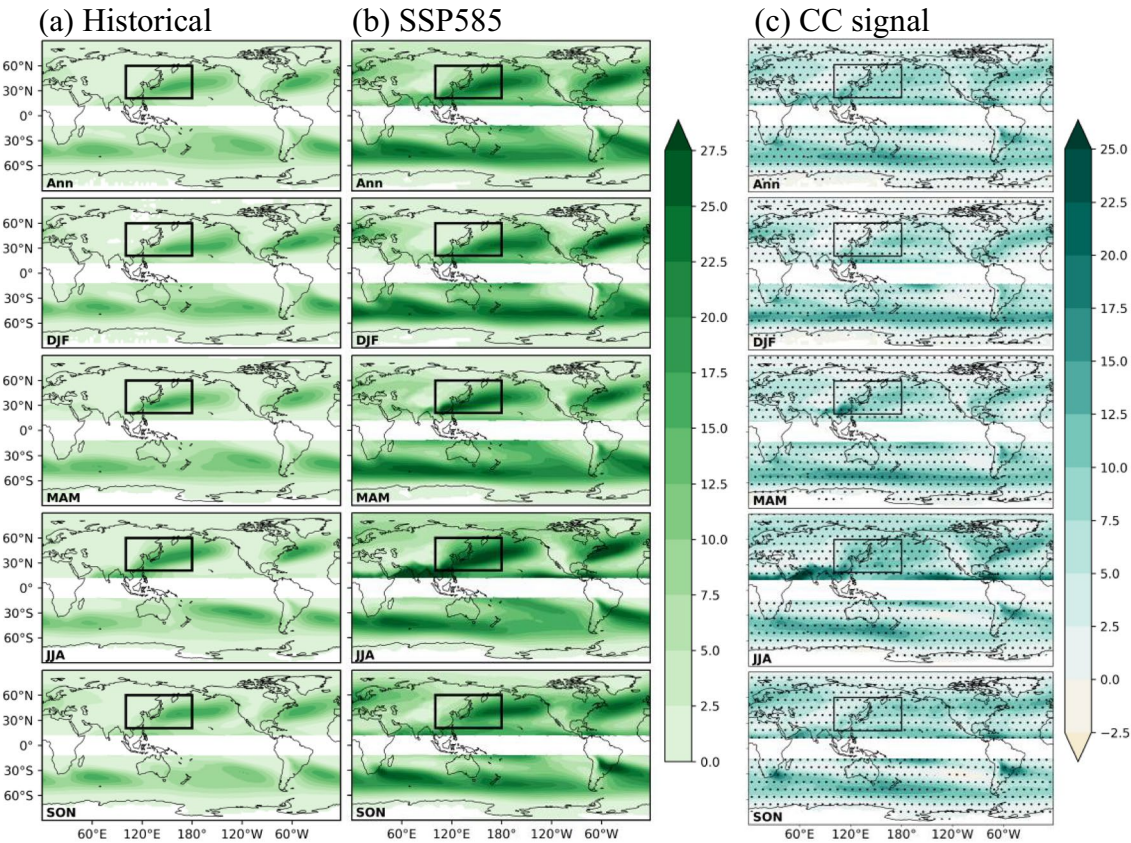


Fig. 1 Annual and seasonal climatology of CMIP6 GCMs ensemble F_{AR} (%) in the (a) historical (1995–2014), (b) SSP585 (2080–2099) period, and (c) CC signal between SSP585 and historical period. The

black boxes represent the mean EA regions used in the study, and the black dots in (c) represent the 95% significant confidence level

Table 3 Statistics of the CMIP6 GCMs ensemble F_{AR} , IVT, PWV, UV, PR, and PR_{ARf} in historical and SSP585 change over GL and EA

	Variable (Units)	Region	Period	Annual	DJF	MAM	JJA	SON
F_{AR} (%)	GL	Historical	3.88	4.03	3.98	4.09	4.06	
		SSP585	+5.42	+4.61	+5.09	+6.78	+5.80	
	EA	Historical	6.40	4.53	6.23	8.90	5.89	
		SSP585	+7.12	+4.60	+7.19	+9.74	+6.89	
	IVT ($\text{kg m}^{-1} \text{s}^{-1}$)	GL	143.9	138.9	138.7	158.0	139.7	
		SSP585	+43.6	+38.9	+40.0	+50.9	+44.7	
PWV (kg m^{-2})	GL	Historical	174.1	123.0	153.9	237.7	180.7	
		SSP585	+56.6	+39.0	+47.9	+81.0	+58.2	
	EA	Historical	18.3	17.1	17.8	20.3	17.9	
		SSP585	+5.9	+5.3	+5.5	+6.8	+6.0	
	UV (m s^{-1})	Historical	20.3	10.6	15.9	33.4	21.0	
		SSP585	+7.5	+3.7	+5.3	+12.6	+8.4	
PR (mm day^{-1})	GL	Historical	8.71	8.79	8.74	8.59	8.70	
		SSP585	-0.04	-0.15	-0.03	+0.03	-0.01	
	EA	Historical	9.31	11.15	9.80	7.15	9.19	
		SSP585	-0.19	-0.06	-0.05	-0.27	-0.39	
	PR _{ARf}	Historical	2.42	2.37	2.40	2.51	2.41	
		SSP585	+0.22	+0.24	+0.22	+0.20	+0.24	
PR _{ARf}	EA	Historical	3.14	2.59	2.72	3.98	3.24	
		SSP585	+0.37	+0.20	+0.31	+0.59	+0.37	
	GL	Historical	0.12	0.13	0.13	0.12	0.13	
		SSP585	+0.11	+0.10	+0.11	+0.13	+0.12	
PR _{ARf}	EA	Historical	0.20	0.15	0.20	0.25	0.20	
		SSP585	+0.15	+0.11	+0.17	+0.16	+0.14	

expected to be higher than the global average (Table 3, GL: +43.6 $\text{kg m}^{-1} \text{s}^{-1}$, EA: +56.6 $\text{kg m}^{-1} \text{s}^{-1}$). The most pronounced increases were projected to occur during the JJA (Table 3, DJF: +39.0 $\text{kg m}^{-1} \text{s}^{-1}$, MAM: +47.9 $\text{kg m}^{-1} \text{s}^{-1}$, JJA: +81.0 $\text{kg m}^{-1} \text{s}^{-1}$, SON: +58.2 $\text{kg m}^{-1} \text{s}^{-1}$). This is in line with the F_{AR} results. However, in contrast with F_{AR} , the most pronounced increase in IVT in EA is likely to occur in the North Pacific region rather than in the southern regions of China (Fig. 2c).

To further analyze future changes in F_{AR} , the influence of moisture and wind elements, which constitute IVT, on future F_{AR} changes were examined. The results of PWV, which is a moisture element of IVT, are presented in Fig. 3. During the historical period, the PWV was highest in tropical regions and decreased with increasing latitudes. Western coastal areas, such as eastern Asia and the eastern United States, situated along the North Pacific and North Atlantic, had higher PWV in JJA and lower values in DJF (Fig. 3a). PWV is anticipated to increase GL and EA (Table 3, GL: +5.9 kg m^{-2} , EA: +7.5 kg m^{-2}). It is projected to increase more significantly in low-latitude areas and mid-latitude boreal summers compared with the historical period (Fig. 3b). This increase in PWV can be explained by the increased capacity of atmospheric water vapor because of

increasing temperatures, as per the Clausius–Clapeyron equation. This could potentially lead to more intense rainfall (Kawo et al. 2023; Ren et al. 2023). The PWV in EA is projected to increase the most during JJA and the least during DJF (Table 3, DJF: +3.7 kg m^{-2} , MAM: +5.3 kg m^{-2} , JJA: +12.6 kg m^{-2} , SON: +8.4 kg m^{-2}), with southern China having the highest increase over land (Fig. 3c).

Figure 4 shows the results for the moist wind component (UV) that constitutes the IVT. During the historical period, UV showed high tendencies in the mid-latitude North Pacific and North Atlantic regions, along with the Antarctic Ocean. The UV in the mid-latitude North Pacific and North Atlantic was strongest during DJF and is closest to the inland areas along the western coast, weakening as it moves eastward through JJA (Fig. 4a). UV is projected to increase the most in the Antarctic Ocean and generally decrease in tropical and mid-latitude oceans (Fig. 4b). In the Antarctic Ocean, a trend of increasing UV, regardless of the season, was noted. Conversely, mid-latitude oceans are predicted to decrease toward the south and increase toward the north. This is particularly the case from approximately 30°N to 40°N, during DJF, MAM, and SON. During JJA, UV in the North Pacific and North Atlantic are expected to decrease. However, an increase was observed below approximately 30°N in the

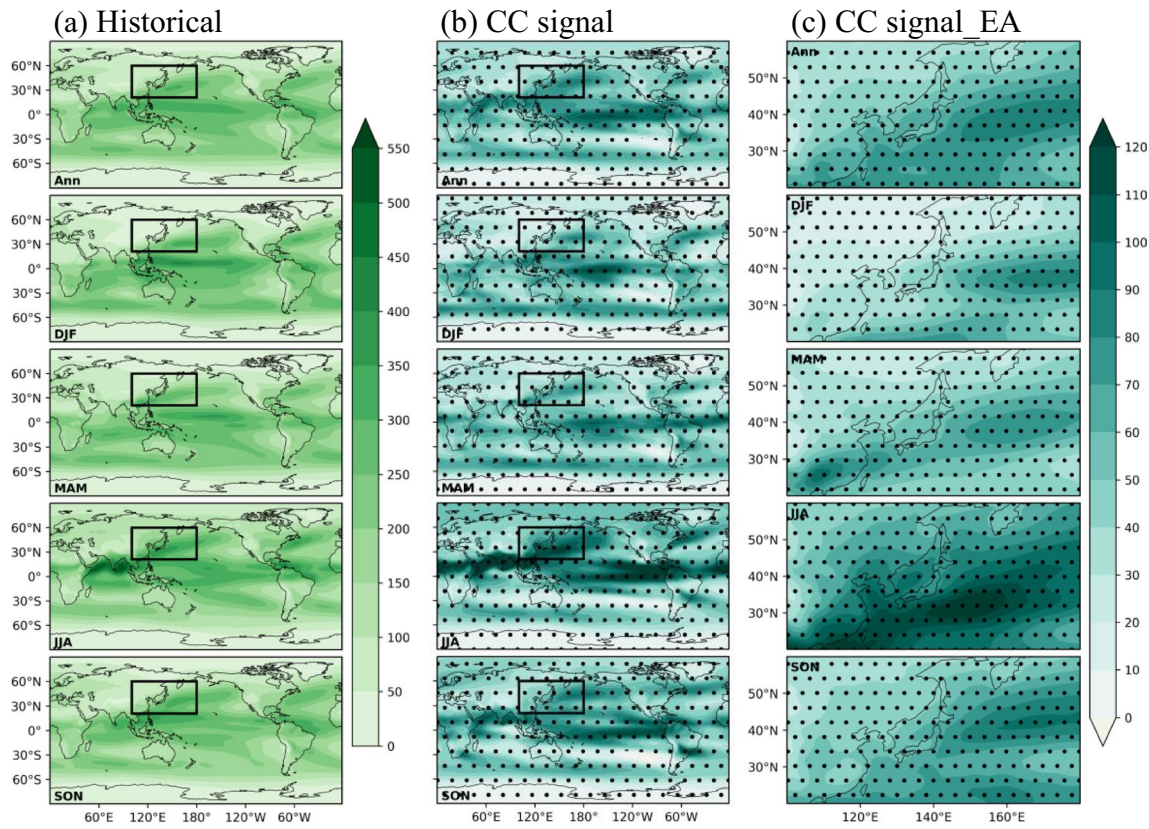


Fig. 2 Annual and seasonal climatology of CMIP6 GCMs ensemble IVT ($\text{kg m}^{-1} \text{s}^{-1}$) in the (a) historical, (b) CC signal between SSP585 and historical period, and (c) is the same as (b) except for EA region.

The black boxes in (a) and (b) represent the EA region used in the study, and the black dots in (c) represent the 95% significant confidence level

Northwest Pacific (Fig. 4b). In EA, the seasonal characteristics of future changes in the mid-latitude North Pacific UV were prominent. During DJF, MAM, and SON, an increase was anticipated toward the north and a decrease toward the south, indicating a poleward movement of UV core (Fig. 4c). It has been studied that the polar movement of future mid-latitude North Pacific UV during DJF, MAM, and SON is related to the polar movement of the mid-latitude storm track (Payne et al. 2020; O'Brien et al. 2022). Meanwhile, during JJA, the pattern was reversed, with an increase anticipated toward the south and a decrease toward the north.

Table 4 shows the pattern correlation coefficient (PCC) results for future changes in the F_{AR} and IVT with respect to the influence of PWV and UV. This section examines which factor, that is, PWV or UV, impacts future variations in F_{AR} and IVT. The PCC between future changes in F_{AR} and PWV had high values across all seasons for the GL and EA regions (GL: 0.453 to 0.596, EA: 0.528 to 0.757). Conversely, the PCC between future changes in F_{AR} and UV showed low values compared to the PCC between future changes in F_{AR} and PWV, except for DJF in GL (GL: 0.339 to 0.495, EA: -0.184 to 0.401). Therefore, the increase in the future F_{AR} is primarily influenced by the increase in the

PWV. This trend is further strengthened in the results for IVT and PWV (GL: 0.620 to 0.816, EA: 0.558 to 0.771), and for IVT and UV (GL: 0.169 to 0.399, EA: -0.446 to 0.453), indicating a strong influence of PWV increase on IVT across all seasons in GL and EA.

We then investigated how future changes in F_{AR} would impact PR. Figure 5 shows the historical period and future changes in PR. PR was generally high in tropical regions, with India and Southeast Asia showing lower PR during DJF and higher concentrations during JJA (Fig. 5a). EA, influenced by the East Asian monsoon, showed noticeable seasonal variations in PR during DJF and JJA (Table 3, DJF: 2.59 mm day^{-1} , JJA: 3.98 mm day^{-1}). In the future, PR is projected to decrease over many oceanic areas between the tropical and mid-latitude zones (Fig. 5b). Within EA, some marine areas showed decreasing trends in PR during DJF, MAM, and SON (Fig. 5c). However, on average, an increase is anticipated in all seasons (Table 3, $+0.20 \text{ mm day}^{-1}$ to $+0.59 \text{ mm day}^{-1}$), particularly showcasing the highest surge during JJA.

Figure 6 presents the results for PR_{ARf} , with additional analysis conducted on the future change ratios of AR-related precipitation (PR_{AR}) and non-AR precipitation (PR_{nonAR}) in

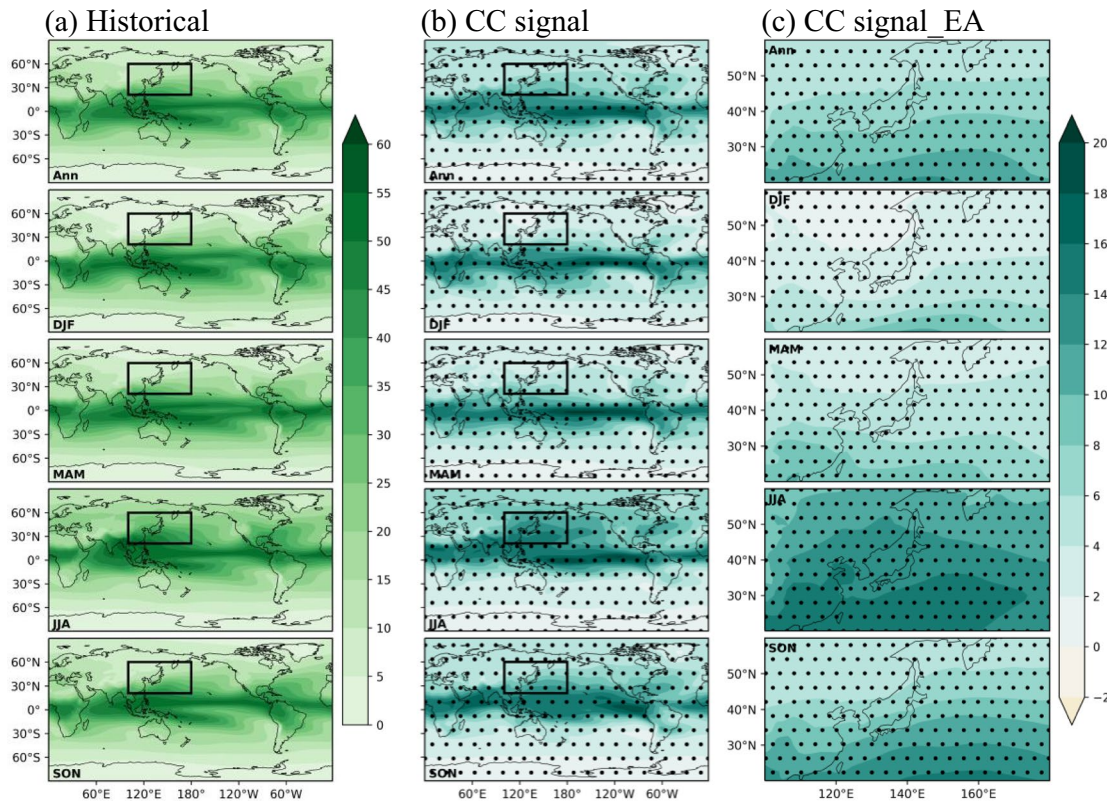


Fig. 3 Same as Fig. 2 except for PWV (kg m^{-2})

EA according to precipitation intensity (Fig. 6d). During the historical period, the position of the core region and its seasonal movement are aligned with the F_{AR} . However, a difference was observed during JJA in the India–Southeast Asia region, where F_{AR} was high but PR_{ARf} was low (Fig. 6a). Future PR_{ARf} is anticipated to increase overall, particularly in the mid-latitude regions (Fig. 6b). For EA, PR_{ARf} is projected to increase overall, showing a greater increase than the global average (Table 3, GL: +0.12, EA: +0.15), especially eastern China in MAM showing the most pronounced increase (Table 3, Fig. 6c). This indicates that the AR will contribute significantly to the overall precipitation in EA. In the future changes in East Asian PR_{AR} and PR_{nonAR} classified by intensity of precipitation (Fig. 6d), PR_{AR} is projected to increase across all precipitation intensities, with a higher rate of increase overall than PR_{nonAR} . This is associated with the increasing PR_{ARf} in EA in the future. Furthermore, it is observed that the proportion of PR_{AR} increases as the intensity of precipitation exceeds 20 mm day^{-1} , indicating a growing influence of extreme PR_{AR} among future PR_{ARf} increases. These results are considered to be associated with the increase in atmospheric moisture capacity because of increase of temperature.

The characteristics and prospects based on AR intensity in EA were investigated. Figure 7 shows the historical (a–e)

and future changes (f–j) in East Asian F_{AR} based on the Ralph et al. (2019) AR category classification. The area-averaged F_{AR} results for EA and its three detailed subregions are presented in Tables 5 and 6. Irrespective of the AR category type, the F_{AR} core was distant from EA during DJF and closer during MAM and JJA, with a seasonal pattern (Fig. 7a–e). The F_{AR} core showed relatively high latitudes for weaker AR and relatively low latitudes for stronger AR (Fig. 7a–e).

By season, ARs with Cat 1 intensity occurred most frequently in DJF, MAM, and SON, whereas ARs with Cat 3 intensity in JJA (Table 5). In terms of the three sub-regions (Table 6), KOR occurred most frequently with Cat 1 intensity in DJF, MAM, and SON and with Cat 3 intensity in JJA. The WJP had similar patterns to KOR but showed a considerable increase in ARs with Cat 4 intensity in JJA. SCN occurred most frequently with Cat 1 intensity in DJF and SON, and ARs with Cat 3 intensity in MAM and JJA, showing distinct features within the EA sub-regions. In future projections (Fig. 7f–j), inland AR occurrences are anticipated to increase regardless of the AR category. Meanwhile, the F_{AR} from Cat 1 to Cat 4 is predicted to decrease in some marine areas and an increase in the F_{AR} of stronger ARs is anticipated in these regions. The pronounced increase in future F_{AR} observed in southern China during MAM and

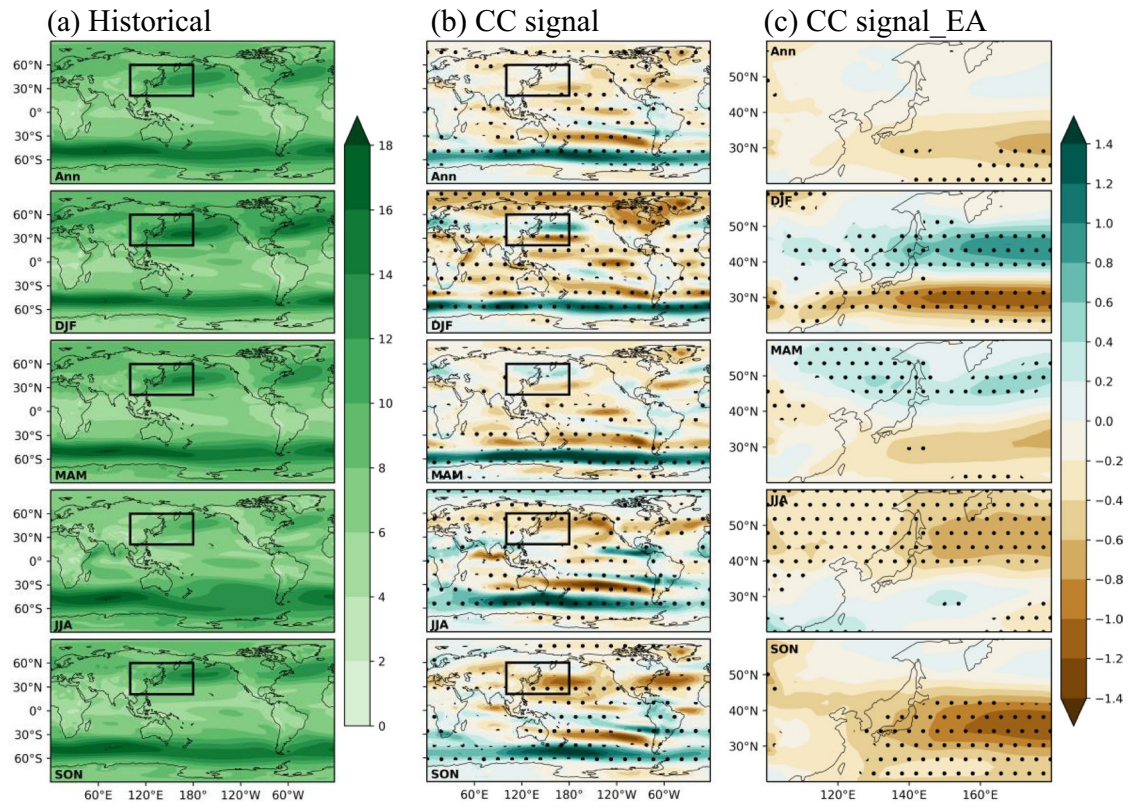


Fig. 4 Same as Fig. 2 except for UV (m s^{-1})

Table 4 PCC results for the future changes in F_{AR} and IVT concerning the influence of PWV and UV over GL and EA

PCC	Region	Annual	DJF	MAM	JJA	SON
$F_{\text{AR}} \& \text{PWV}$	GL	0.516	0.453	0.473	0.596	0.505
	EA	0.704	0.757	0.613	0.690	0.528
$F_{\text{AR}} \& \text{UV}$	GL	0.391	0.495	0.416	0.339	0.355
	EA	-0.220	-0.184	-0.176	0.401	-0.174
IVT & PWV	GL	0.732	0.620	0.654	0.816	0.735
	EA	0.706	0.748	0.558	0.771	0.599
IVT & UV	GL	0.232	0.399	0.328	0.217	0.169
	EA	-0.369	-0.089	-0.230	0.453	-0.446

JJA (Fig. 1c) was mainly attributed to the increase in F_{AR} of Cat 3 or higher intensities. The highest F_{AR} increase in EA occurred during Cat 5 intensity in JJA (Table 5). This was mainly from southern inland China through southern Japan to the western North Pacific, with the highest increase (over +10%) in southern Japan (Fig. 7j). All three sub-regions showed a future increase in F_{AR} in all seasons and AR intensities, with the highest increase in F_{AR} in Cat 5 intensity during JJA. However, the greatest increase in F_{AR} differed among the sub-regions, with the highest expected increase in Cat 5 intensities during JJA in KOR and WJP (KOR: +3.90%, WJP: +5.93%) and Cat 4 intensity during MAM in SCN (+6.19%) (Table 6).

The variations in water vapor transport by the AR and changes in precipitation were examined based on the seasonal variations of the East Asian summer monsoon through the Hovmöller diagram of the longitudinal range in the KOR region (124.5°E to 130.5°E). Figure 8 shows the Hovmöller diagrams for F_{AR} (Fig. 8a–c), IVT (Fig. 8d–f), and PR (Fig. 8g–i) for the historical period, future, and future changes. During the historical period, F_{AR} expanded poleward from January to July and then contracted after August, with a peak near 30°N around June (Fig. 8a). In the future, F_{AR} is projected to increase overall, particularly below 30°N from April to June and around 35°N to 50°N in July, intensifying the core of F_{AR} and the poleward extension in

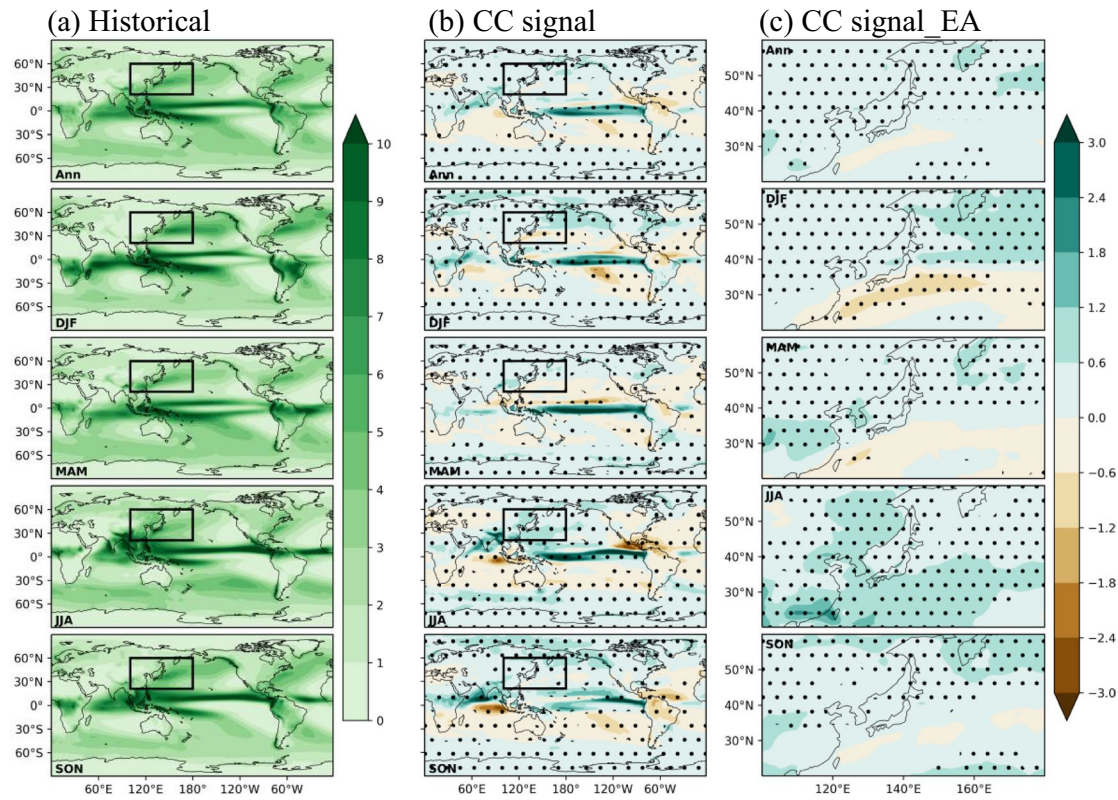


Fig. 5 Same as Fig. 2 except for precipitation (mm day^{-1})

July (Fig. 8b–c). The IVT followed a similar pattern to the F_{AR} , increasing from January to July before decreasing and contracting after August, with a peak near 30°N in June (Fig. 8d). The future IVT showed an overall increasing trend, notably from below 30°N in June to approximately 45°N in July (Fig. 8e–f). PR shows seasonal variability akin to F_{AR} and IVT. However, there was a difference in the location of the core, because it appears near 30°N in June, 40°N in July, and 20°N in August (Fig. 8g). In the future, the PR will generally increase, except for a decrease below 35°N in late winter to spring, with the most pronounced increases occurring in June, July, and August. This matches the latitude positions of the PR cores during those months (Fig. 8h–i). Summarizing the results for these variables, IVT and F_{AR} exhibited a northward movement resembling the East Asian summer monsoon rainband from late spring to early summer. Future predictions show that F_{AR} , IVT, and PR will increase simultaneously in June and July. This is expected to strengthen the water vapor transport and precipitation related to the East Asian summer monsoon.

Figure 9 shows the results for the AR categories using the same method as shown in Fig. 8. During the historical period (Fig. 9a–e), weaker AR occurred at higher latitudes, whereas stronger AR occurred primarily at lower latitudes in JJA. The F_{AR} cores were located at 30°N for both the weaker

and stronger AR. However, the weaker the AR, the more it occurred in MAM, and the stronger the AR, the more it occurred in JJA. In the future (Fig. 9f–j), regardless of the AR intensity, AR is expected to occur at latitudes higher than those where AR occurred in the historical period. F_{AR} cores are expected to form earlier and have higher frequencies than in the historical period. ARs with Cat 1, Cat 2, and Cat 3 intensities are expected to decrease around the 30°N region in MAM or JJA when F_{AR} cores of the historical period exist (Fig. 9k–o). However, at these times and locations, there was a considerable increase in F_{AR} with Cat 4 or Cat 5 intensity. The intensity of AR during the East Asian summer monsoon period is likely to increase.

4 Summary and Conclusions

This study used MME of 15 models participating in CMIP6 to conduct projections for AR and AR-related elements globally and in EA. The analysis covered a span of 20 years for the far future (2080–2099) under the SSP5-8.5 scenario and the historical period (1995–2014). The AR detection scheme of Park et al. (2021) was used to identify ARs, and the ensemble results were computed using 15 GCMs.

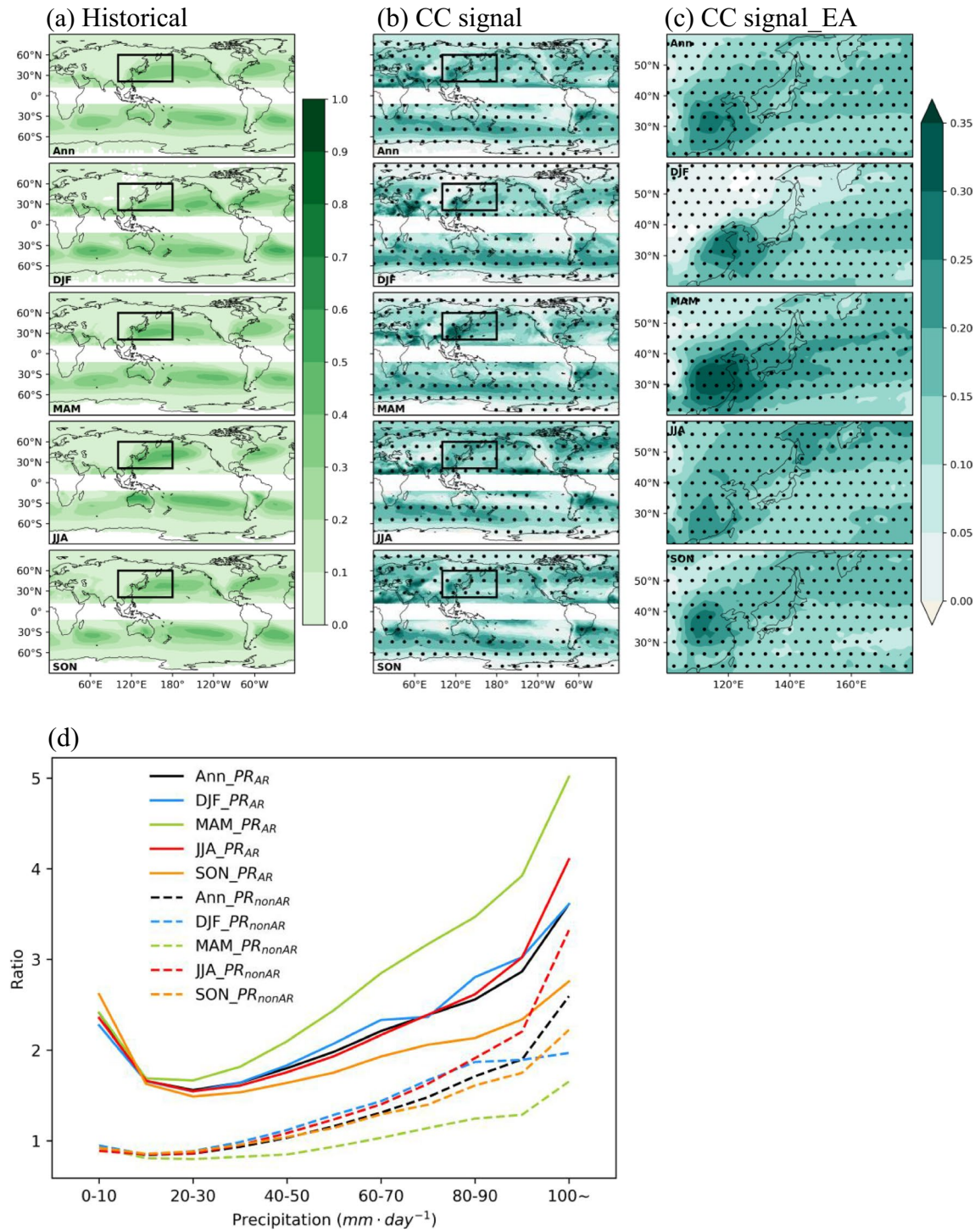


Fig. 6 (a-c) are same as Fig. 2 except for PR_{ARf}. (d) means the future change ratio of PR_{AR} and PR_{nonAR} in EA according to precipitation intensity

AR prominently occurred in mid-latitude regions of the North Pacific and North Atlantic, and in the Antarctic seas. EA was influenced by AR, predominantly during MAM and JJA. Future F_{AR} is expected to increase, with EA exhibiting a greater increase in F_{AR} than the global mean. EA is

expected to experience the most pronounced increase during summer. For mid-latitude regions, IVT showed spatial and seasonal patterns similar to those of F_{AR} in both historical and future periods. However, unlike F_{AR}, IVT appears prominently in tropical maritime regions in both historical

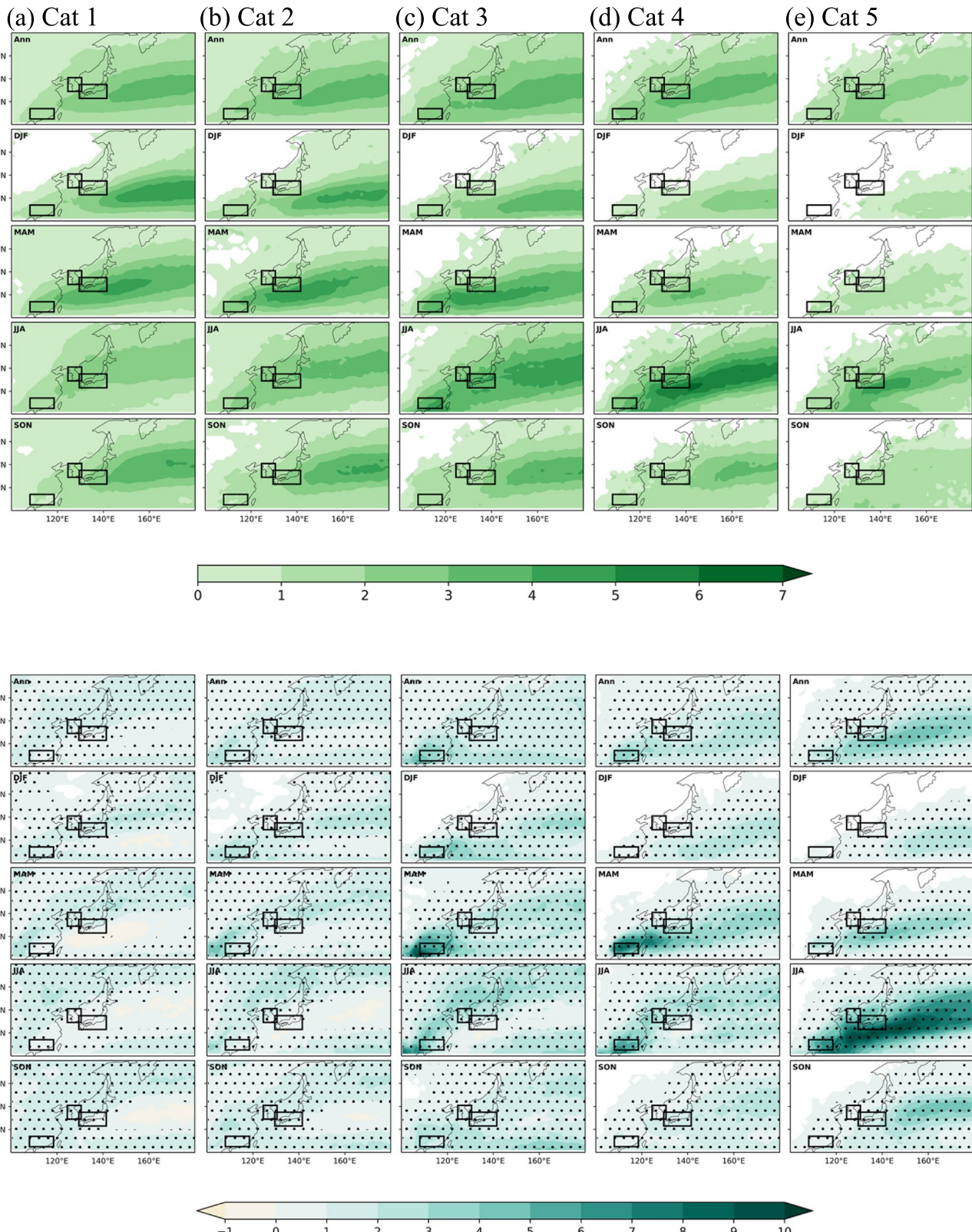


Fig. 7 Annual and seasonal climatology of F_{AR} (%) according to AR category in the historical (a–e), and CC signal between SSP585 and historical period (f–j). (a–e) and (f–j) mean each AR categories 1–5.

The black boxes represent the KOR, WJP, and SCN regions, and the black dots in (f–j) represent the 95% significant confidence level

Table 5 F_{AR} (%) according to AR category in historical and SSP585 change over EA

Period	Variable	Annual	DJF	MAM	JJA	SON
Historical	Cat 1	1.34	1.17	1.46	1.41	1.34
	Cat 2	1.28	0.97	1.37	1.55	1.22
	Cat 3	1.30	0.78	1.28	2.04	1.09
	Cat 4	0.88	0.35	0.56	1.87	0.71
	Cat 5	0.37	0.08	0.10	0.98	0.34
SSP585	Cat 1	+0.97	+0.73	+0.99	+1.00	+1.14
	Cat 2	+1.11	+0.85	+1.17	+1.22	+1.18
	Cat 3	+1.44	+0.96	+1.56	+1.88	+1.34
	Cat 4	+1.14	+0.63	+1.38	+1.68	+0.87
	Cat 5	+1.31	+0.42	+0.86	+2.95	+0.99

Table 6 Same as Table 5, except for KOR, WJP, SCN region

Region	Period	Variable	Annual	DJF	MAM	JJA	SON
KOR	Historical	Cat 1	1.35	0.39	1.58	2.14	1.24
		Cat 2	1.16	0.14	1.21	2.35	0.90
		Cat 3	1.12	0.07	0.94	2.73	0.73
		Cat 4	0.75	0.00	0.39	2.29	0.28
		Cat 5	0.32	0.00	0.05	1.14	0.07
	SSP585	Cat 1	+1.08	+0.95	+1.51	+0.48	+1.38
		Cat 2	+1.14	+0.70	+1.61	+1.01	+1.25
		Cat 3	+1.37	+0.32	+1.61	+2.32	+1.23
		Cat 4	+1.13	+0.08	+1.09	+2.66	+0.67
		Cat 5	+1.30	0.00	+0.75	+3.90	+0.50
WJP	Historical	Cat 1	2.22	1.36	3.11	2.25	2.15
		Cat 2	2.15	0.78	2.95	2.80	2.04
		Cat 3	2.07	0.49	2.40	3.75	1.59
		Cat 4	1.52	0.07	1.14	4.03	0.82
		Cat 5	0.81	0.01	0.19	2.60	0.41
	SSP585	Cat 1	+0.82	+1.41	+0.79	+0.15	+0.92
		Cat 2	+1.03	+1.23	+1.39	+0.36	+1.16
		Cat 3	+1.34	+0.88	+1.94	+1.02	+1.53
		Cat 4	+1.45	+0.48	+2.33	+1.63	+1.36
		Cat 5	+2.38	+0.11	+2.11	+5.93	+1.32
SCN	Historical	Cat 1	1.52	1.31	2.26	1.59	0.90
		Cat 2	1.62	1.22	2.40	1.99	0.83
		Cat 3	2.13	0.92	2.98	3.69	0.89
		Cat 4	1.06	0.07	0.92	2.82	0.39
		Cat 5	0.31	0.00	0.07	0.95	0.19
	SSP585	Cat 1	+0.93	+1.31	+0.81	+0.51	+1.11
		Cat 2	+1.64	+2.24	+1.87	+0.99	+1.47
		Cat 3	+3.52	+2.82	+6.08	+3.10	+2.07
		Cat 4	+3.16	+0.38	+6.19	+5.09	+0.91
		Cat 5	+1.97	+0.03	+1.62	+5.49	+0.67

and future periods. IVT in EA is projected to increase more significantly than the global average, with the most prominent increase expected during JJA in the northwestern Pacific region. When dividing IVT into humidity-related components (PWV) and moist wind components (UV) and

examining the impact of each component on the future changes of IVT and F_{AR} , the future IVT increase in global and EA is primarily associated with PWV increase. This feature was also observed in F_{AR} . The spread between models regarding F_{AR} and IVT is largely influenced by wind (Kim

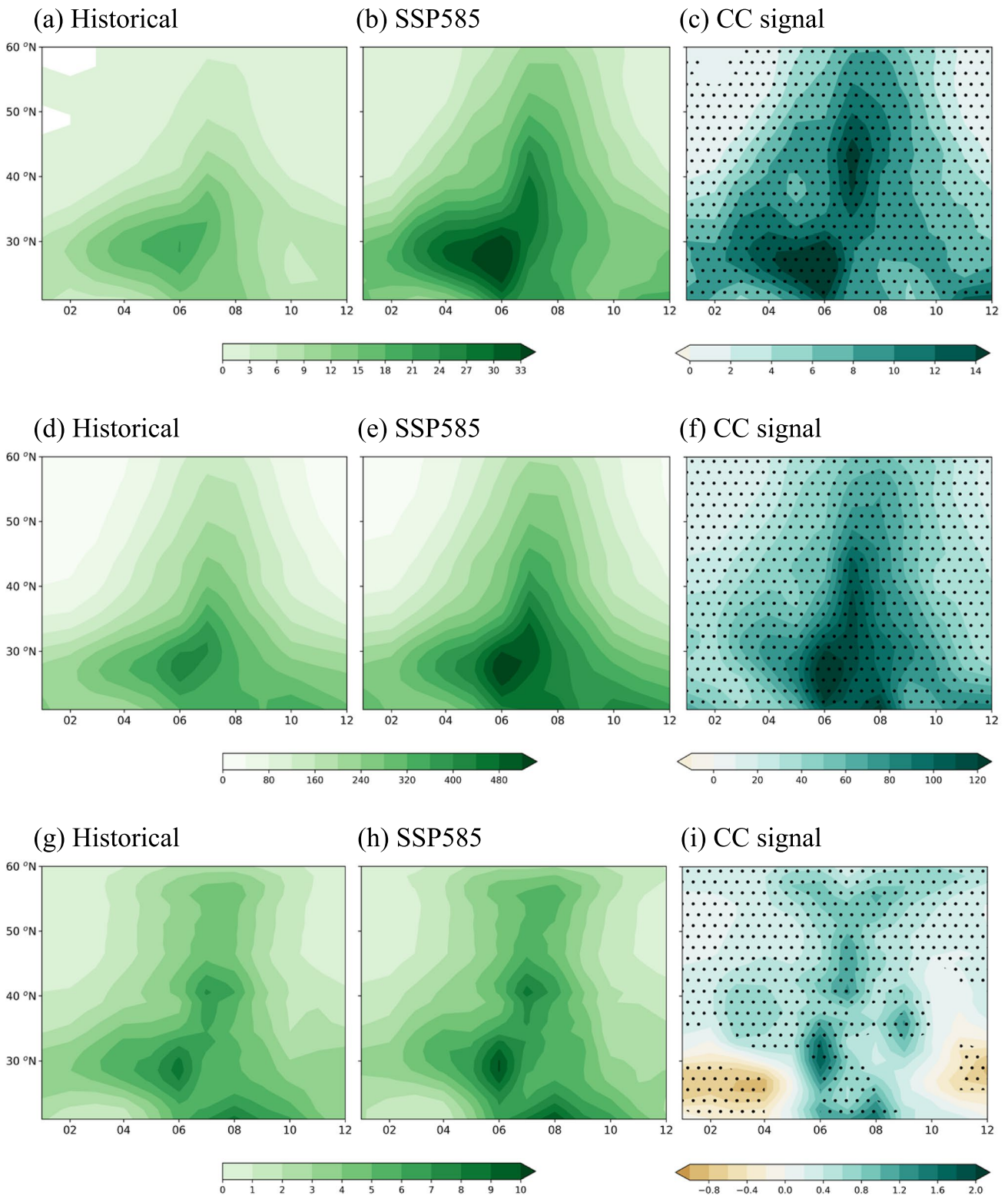


Fig. 8 The Hovmöller diagram of the seasonal–meridional variations of F_{AR} (%), a to c), IVT ($\text{kg m}^{-1} \text{s}^{-1}$, d to f), and precipitation (mm day^{-1} , g to i) over the longitude range corresponding to the Korean Peninsula, 124.5°E to 130.5°E , from CMIP6 GCMs ensemble. (a),

(d), (g) mean historical period, (b), (e), (h) mean SSP585. (c), (f), (i) mean CC signal between SSP585 and historical period, and the black dots represent the 95% significant confidence level

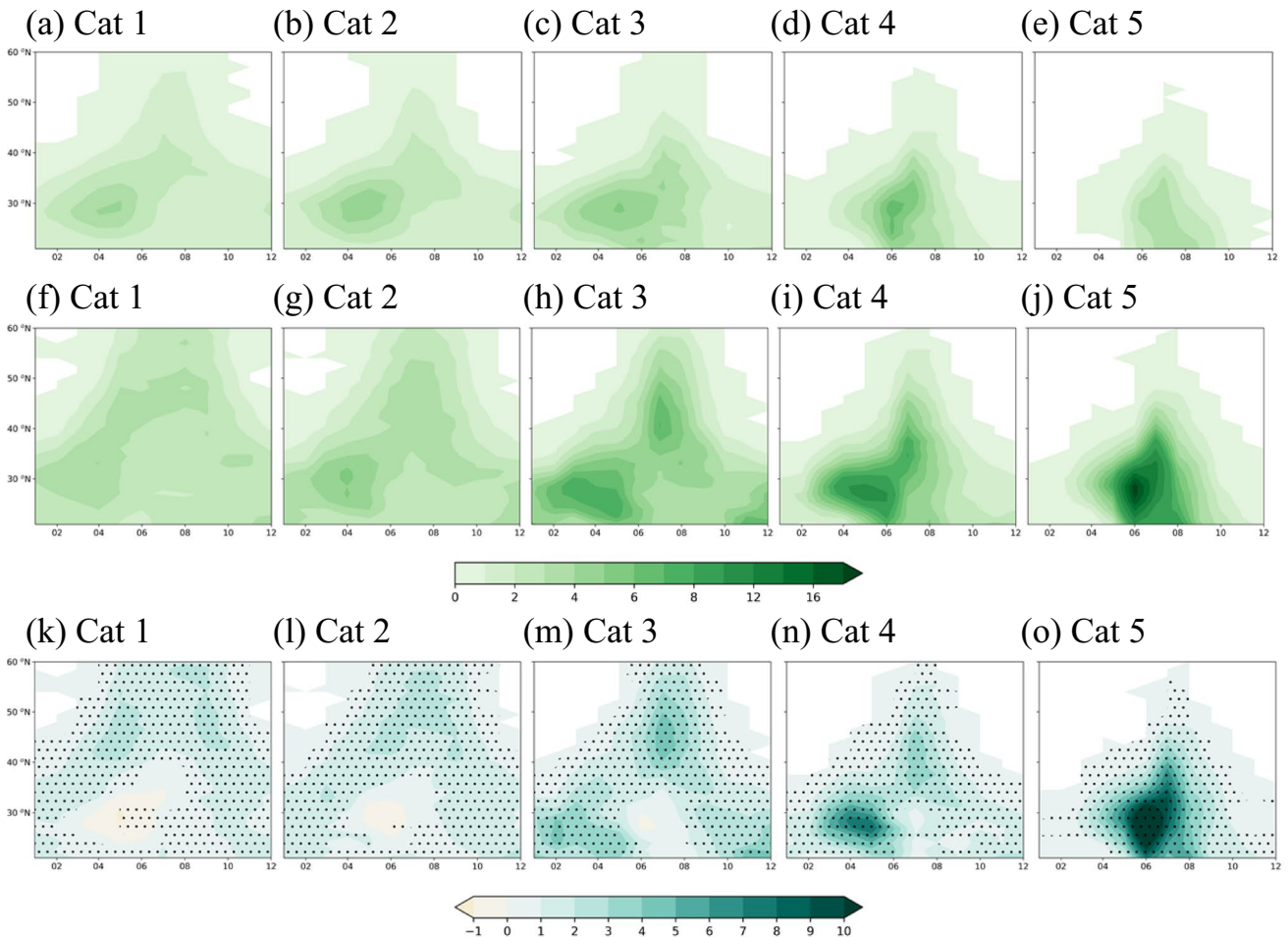


Fig. 9 Same as Fig. 8, except for AR category (%). (a–e) mean historical period, (f–j) mean SSP585, and (k–o) mean CC signal between SSP585 and historical period, and the black dots represent the 95% significant confidence level

et al. 2023b); however, for future changes, the contribution of humidity presents a more significant difference.

The next step was to investigate how future changes in F_{AR} would impact PR. The PR was high in tropical regions during this historical period. In EA, the PR was higher during JJA and lower during DJF. In future, the most prominent increase in PR is expected in the tropical Pacific region. In EA, PR showed an increasing trend, except in specific maritime areas. And PR is expected to increase most prominently in JJA, leading to an anticipated rise in the seasonal variability of PR. During the historical period, PR_{ARf} exhibited a distribution similar to that of F_{AR} . PR_{ARf} is expected to increase overall, with particularly pronounced increases anticipated in the mid-latitude regions. The changes in PR_{ARf} are expected to be strongly influenced by the increase in PR_{AR} , with a significant increase anticipated in extreme PR_{AR} .

When classifying F_{AR} in EA based on the duration of AR and maximum IVT, Cat 1 AR, the weakest intensity, mainly occurred in DJF, MAM, and SON, whereas Cat 3

AR, the moderate intensity, occurred most frequently during JJA. In the future, the F_{AR} of inland areas is expected to increase irrespective of the intensity and season of AR. In terms of seasonality, F_{AR} in DJF, MAM, and SON was expected to increase the most significantly in AR of Cat 3 intensity. Meanwhile, F_{AR} in JJA was expected to have the highest increase in ARs with Cat 5 intensity. However, within EA, owing to geographical differences, the seasons and AR intensities in which F_{AR} is expected to increase varied most prominently by region.

Analysis of the seasonal variations in F_{AR} , IVT, and PR along the longitude corresponding to the Korean Peninsula using the Hovmöller diagram showed that from late spring to early summer, the changes in IVT and F_{AR} exhibited a trend similar to the northward movement of the East Asian summer monsoon precipitation belt. This suggests a close relationship between moisture transport by the AR and precipitation during the East Asian summer monsoon season. IVT, F_{AR} , and PR are expected to increase during June and July in the future. Therefore, the influence of

ARs on water vapor transport and precipitation is expected to increase during the future East Asian summer monsoon season. When F_{AR} is classified by AR categories, F_{AR} cores tend to appear more in spring for weaker ARs and in summer for stronger ARs. The occurrence of strong intensity AR is expected to increase during the East Asian summer monsoon season.

The SSP5-8.5 scenario-based projections of AR in EA presented in this study can serve as a valuable reference for future research on AR projections in the region. However, because AR projections vary depending on future scenarios (Liang and Haywood 2023), it is necessary to present AR projection information based on various scenarios. Additionally, since the timing and impact of AR and AR-related precipitation vary by region within EA (Kim et al. 2023a), more detailed studies tailored to regional characteristics are needed.

Acknowledgements This work was funded by the Korea Meteorological Administration Research and Development Program "Developing and Assessing Climate Change Scenarios" under Grant (KMA2018-00321).

Declarations

Competing Interests The authors declare that they have no conflict of interest.

References

- Albano, C.M., Dettinger, M.D., Happold, A.A.: Patterns and drivers of atmospheric river precipitation and hydrologic impacts across the western United States. *J. Hydrometeorol.* **21**, 143–159 (2020). <https://doi.org/10.1175/JHM-D-19-0119.1>
- Allan, R.P., Liu, C., Zahn, M., Lavers, D.A., Koukouvas, E., Bodas-Salcedo, A.: Physically consistent responses of the global atmospheric hydrological cycle in models and observations. *Surv. Geophys.* **35**, 533–552 (2014). <https://doi.org/10.1007/s10712-012-9213-z>
- Benedict, I., Ødemarck, K., Nipen, T., Moore, R.: Large-scale flow patterns associated with extreme precipitation and atmospheric rivers over Norway. *Mon. Weather Rev.* **147**, 1415–1428 (2019). <https://doi.org/10.1175/MWR-D-18-0362.1>
- Corrington, T.W., McCarthy, J., Shulgina, T., Gershunov, A., Cayan, D.R., Ralph, F.M.: Climate change contributions to future atmospheric river flood damages in the western United States. *Sci. Rep.* **12**, 13747 (2022). <https://doi.org/10.1038/s41598-022-15474-2>
- DeFlorio, M.J., Waliser, D.E., Guan, B., Ralph, F.M., Vitart, F.: Global evaluation of atmospheric river subseasonal prediction skill. *Clim. Dyn.* **52**, 3039–3060 (2019). <https://doi.org/10.1007/s00382-018-4309-x>
- Dettinger, M.D.: Climate change, atmospheric rivers, and floods in California – a multimodel analysis of storm frequency and magnitude changes. *J. Am. Water Resour. Assoc.* **47**, 514–523 (2011). <https://doi.org/10.1111/j.1752-1688.2011.00546.x>
- Dettinger, M.D.: Atmospheric rivers as drought busters on the U. S. West Coast. *J. Hydrometeorol.* **14**, 1721–1732 (2013). <https://doi.org/10.1175/JHM-D-13-02.1>
- Dettinger, M.D., Ralph, F.M., Das, T., Neima, P.J., Cayan, D.R.: Atmospheric rivers, floods and the water resources of California. *Water* **3**, 445–478 (2011). <https://doi.org/10.3390/w3020445>
- Espinoza, V., Waliser, D.E., Guan, B., Lavers, D.A., Ralph, F.M.: Global analysis of climate change projection effects on atmospheric rivers. *Geophys. Res. Lett.* **45**, 4299–4308 (2018). <https://doi.org/10.1029/2017GL076968>
- Gao, Y., Lu, J., Leung, L.R.: Uncertainties in projecting future changes in atmospheric rivers and their impacts on heavy precipitation over Europe. *J. Clim.* **29**, 6711–6726 (2016). <https://doi.org/10.1175/JCLI-D-16-0088.1>
- Guan, B., Waliser, D.E.: Detection of atmospheric rivers: Evaluation and application of an algorithm for global studies. *J. Geophys. Res. Atmos.* **120**, 12514–12535 (2015). <https://doi.org/10.1002/2015jd024257>
- Guan, B., Waliser, D.E.: Tracking atmospheric rivers globally: Spatial distributions and temporal evolution of life cycle characteristics. *J. Geophys. Res. Atmos.* **124**, 12523–12552 (2019). <https://doi.org/10.1029/2019JD031205>
- Ionita, M., Nagaviciu, V., Guan, B.: Rivers in the sky, flooding on the ground: the role of atmospheric rivers in inland flooding in central Europe. *Hydrol. Earth Syst. Sci.* **24**, 5125–5147 (2020). <https://doi.org/10.5194/hess-24-5125-2020>
- Ishida, K., Kavvas, M.L., Chen, Z.Q.R., Dib, A., Diaz, A.J., Anderson, M.L.: Physically based maximum precipitation estimation under future climate change conditions. *Hydrol. Process.* **32**, 3188–3201 (2018). <https://doi.org/10.1002/hyp.13253>
- Jeon, S., PrabhatByna, S., Ju, J., Collins, W.D., Wehner, M.F.: Characterization of extreme precipitation within atmospheric river events over California. *Adv. Stat. Clim. Meteorol. Oceanogr.* **1**, 45–57 (2015). <https://doi.org/10.5194/ascmo-1-45-2014>
- Kamae, Y., Mei, W., Xie, S.: Climatological relationship between warm season atmospheric rivers and heavy rainfall over East Asia. *J. Meteor. Soc. Japan.* **95**, 411–431 (2017). <https://doi.org/10.2151/jmsj.2017-027>
- Kamae, Y., Mei, W., Xie, S., Naoi, M., Ueda, H.: Atmospheric rivers over the northwestern Pacific: Climatology and interannual variability. *J. Clim.* **30**, 5605–5619 (2017). <https://doi.org/10.1175/JCLI-D-16-0875.1>
- Kawo, Al., Schaebybroeck, B.V., Malderen, R.V., Pottiaux, E.: Precipitable water vapor in regional climate models over Ethiopia: model evaluation and climate projections. *Clim. Dyn.* **61**, 5287–5307 (2023). <https://doi.org/10.1007/s00382-023-06855-y>
- Kim, J., Waliser, D.E., Neiman, P.J., Guan, B., Ryoo, J., Wick, G.A.: Effects of atmospheric river landfalls on the cold season precipitation in California. *Clim. Dyn.* **40**, 465–474 (2013). <https://doi.org/10.1007/s00382-2012-1322-3>
- Kim, J., Moon, H., Guan, B., Waliser, D.E., Choi, J., Gu, T.-Y., Byun, Y.-H.: Precipitation characteristics related to atmospheric rivers in East Asia. *Int. J. Climatol.* **41**, E2244–E2257 (2021). <https://doi.org/10.1002/joc.6843>
- Kim, J., Kim, T.-J., Kim, J.-U., Chung, C.-Y., Byun, Y.-H.: Evaluation of CMIP6 GCMs for simulating atmospheric rivers: Relating the model skill for key AR variables to the skill for winds and water vapor. *Asia-Pac. J. Atmos. Sci.* (2023a). <https://doi.org/10.1007/s13143-023-00342-4>
- Kim, T.-J., Kim, J., Park, C., Son, S.-W., Kim, J.-U., Kwon, S.-H., Moon, H., Byun, Y.-H.: Evaluation of a CMIP6 multi-GCM ensemble for atmospheric rivers and precipitation over East Asia. *Asia-Pac. J. Atmos. Sci.* **59**, 327–345 (2023). <https://doi.org/10.1007/s13143-022-0031103>
- Lavers, D. A., Allan, R. P., Villarini, G., Lloyd-Hughes, B., Brayshaw, D. J., Wade, A. J.: Future changes in atmospheric rivers and their implications for winter flooding in Britain. *Environ. Res. Lett.* **8**, 034010 (2013). <https://doi.org/10.1088/1748-9326/8/3/034010>

- Lavers, D.A., Ralph, F.M., Waliser, D.E., Gershunov, A., Dettinger, M.D.: Climate change intensification of horizontal water vapor transport in CMIP5. *Geophys. Res. Lett.* **42**, 5617–5625 (2015). <https://doi.org/10.1002/2015GL064672>
- Leung, L.R., Qian, Y.: Atmospheric rivers induced heavy precipitation and flooding in the western US simulated by the WRF regional climate model. *Geophys. Res. Lett.* **36**, L03820 (2009). <https://doi.org/10.1029/2008GL036445>
- Liang, J., Haywood, J.: Future changes in atmospheric rivers over East Asia under stratospheric aerosol intervention. *Atmos. Chem. Phys.* **23**, 1687–1703 (2023). <https://doi.org/10.5194/acp-23-1687-2023>
- Liang, J., Yong, Y., Hawcroft, M.K.: long-term trends in atmospheric rivers over East Asia. *Clim. Dyn.* **60**, 643–666 (2023). <https://doi.org/10.1007/s00382-022-06339-5>
- Mahoney, K., Swales, D., Mueller, M.J., Alexander, M., Hughes, M., Malloy, K.: An examination of an inland-penetrating atmospheric river flood event under potential future thermodynamic conditions. *J. Clim.* **31**, 6281–6297 (2018). <https://doi.org/10.1175/JCLI-D-18-0118.1>
- Meresa, H., Tischbein, B., Mekonnen, T.: Climate change impact on extreme precipitation and peak flood magnitude and frequency: observations from CMIP6 and hydrological models. *Nat. Hazards* **111**, 2649–2679 (2022). <https://doi.org/10.1007/s11069-021-05152-3>
- Neiman, P.J., Ralph, F.M., Wick, G.A., Lundquist, J., Dettinger, M.D.: Meteorological characteristics and overland precipitation impacts of atmospheric rivers affecting the West Coast of North America based on eight years of SSM/I satellite observations. *J. Hydrometeorol.* **9**, 22–47 (2008). <https://doi.org/10.1175/2007JHM855.1>
- O'Brien, T. A., Wehner, M. F., Payne, A. E., Shields, C. A., Rutz, J. J., Leung, L.-R., Ralph, F. M., Collow, A., Gorodetskaya, I., Guan, B., Lora, J. M., McClenney, E., Nardi, K. M., Ramos, A. M., Tomé, R., Sarangi, C., Shearer, E. J., Ullrich, P. A., Zarzycki, C., Loring, B., Huang, H., Inda-Díaz, H. A., Rhoades, A. M., Zhou, Y.: Increases in future AR count and size: Overview of the ART-MIP Tier 2 CMIP5/6 Experiment. *J. Geophys. Res. Atmos.* **127**, e2021JD036013 (2022). <https://doi.org/10.1029/2021JD036013>
- Paltan, H., Waliser, D., Lim, W.H., Guan, B., Yamazaki, D., Pant, R., Dadson, S.: Global floods and water availability driven by atmospheric rivers. *Geophys. Res. Lett.* **44**, 10387–10395 (2017). <https://doi.org/10.1002/2017GL074882>
- Pan, M., Lu, M.: East Asia atmospheric river catalog: Annual cycle, transition mechanism, and precipitation. *Geophys. Res. Lett.* **47**, e2020GL089477 (2020). <https://doi.org/10.1029/2020GL089477>
- Park, C., Son, S.-W., Kim, H.: Distinct features of atmospheric rivers in the early versus late east Asian summer monsoon and their impacts on monsoon rainfall. *J. Geophys. Res. Atmos.* **126**, e2020JD033537 (2021). <https://doi.org/10.1029/2020JD033537>
- Park, C., Son, S.-W., Guan, B.: Multiscale nature of atmospheric rivers. *Geophys. Res. Lett.* **50**, e2023GL102784 (2023). <https://doi.org/10.1029/2023GL102784>
- Payne, A.E., Demory, M.-E., Leung, L.R., Ramos, A.M., Shields, C.A., Rutz, J.J., Ralph, F.M.: Responses and impacts of atmospheric rivers to climate change. *Nat. Rev. Earth Environ.* **1**, 143–157 (2020). <https://doi.org/10.1038/s43017-020-0030-5>
- Ralph, F.M., Neiman, P.J., Wick, G.A., Gutman, S.I., Dettinger, M.D., Cayan, D.R., White, A.B.: Flooding on California's Russian River: Role of atmospheric rivers. *Geophys. Res. Lett.* **33**, L13801 (2006). <https://doi.org/10.1029/2006GL026689>
- Ralph, F.M., Rutz, J.J., Cordeira, J.M., Dettinger, M., Anderson, M., Reynolds, D., Schick, L.J., Smallcomb, C.: A scale to characterize the strength and impacts of atmospheric rivers. *Bull. Am. Meteorol. Soc.* **100**, 269–289 (2019). <https://doi.org/10.1175/BAMS-D-18-0023.1>
- Ren, D., Wang, Y., Wang, G., Liu, L.: Rising trends of global precipitable water vapor and its correlation with flood frequency. *Geod. Geodyn.* **14**, 355–367 (2023). <https://doi.org/10.1016/j.geog.2022.12.001>
- Rhoades, A.M., Risser, M.D., Stone, D.A., Wehner, M.F., Jones, A.D.: Implications of warming on western United States landfalling atmospheric rivers and their flood damages. *Weather and Clim. Extremes* **32**, 100326 (2021). <https://doi.org/10.1016/j.wace.2021.100326>
- Rutz, J.J., Steenburgh, W.J., Ralph, F.M.: Climatological characteristics of atmospheric rivers and their inland penetration over the western United States. *Mon. Wea. Rev.* **142**, 905–921 (2014). <https://doi.org/10.1175/MWR-D-13-00168.1>
- Ryu, Y., Moon, H., Kim, J., Kim, T.-J., Boo, K.-O., Guan, B., Kamae, Y., Mei, W., Park, C., Son, S.-W., Byun, Y.-H.: A multi-inventory ensemble analysis of the effects of atmospheric rivers on precipitation and streamflow in the Namgang-Dam basin in Korea. *Water. Resour. Res.* **57**, e2021WR030058 (2021). <https://doi.org/10.1029/2021WR030058>
- Wang, S., Ma, X., Zhou, S., Wu, L., Wang, H., Tang, Z., Xu, G., Jing, Z., Chen, Z., Gan, B.: Extreme atmospheric rivers in a warming climate. *Nat. Commun.* **14**, 3219 (2023). <https://doi.org/10.1038/s41467-023-38980-x>
- Whan, K., Sillmann, J., Schaller, N., Haarsma, R.: Future changes in atmospheric rivers and extreme precipitation in Norway. *Clim. Dyn.* **54**, 2071–2084 (2020). <https://doi.org/10.1007/s00382-019-05099-z>
- Zhang, L., Zhao, Y., Cheng, T. F., Gu, M.: Future changes in global atmospheric rivers projected by CMIP6 models. *J. Geophys. Res. Atmos.* **129**, e2023JD039359 (2024). <https://doi.org/10.1029/2023JD039359>
- Zhu, Y., Newell, R.E.: A proposed algorithm for moisture fluxes from atmospheric rivers. *Mon. Weather. Rev.* **126**, 725–735 (1998). [https://doi.org/10.1175/1520-0493\(1998\)126%3c0725:APAFMF%3e2.0.CO;2](https://doi.org/10.1175/1520-0493(1998)126%3c0725:APAFMF%3e2.0.CO;2)

Publisher's Note Springer Nature remains neutral with regard to jurisdictional claims in published maps and institutional affiliations.

Springer Nature or its licensor (e.g. a society or other partner) holds exclusive rights to this article under a publishing agreement with the author(s) or other rightsholder(s); author self-archiving of the accepted manuscript version of this article is solely governed by the terms of such publishing agreement and applicable law.